

Triggered Population III star formation: the effect of H₂ self-shielding

Gen Chiaki^{1,2,3*} and John H. Wise¹

¹Center for Relativistic Astrophysics, School of Physics, Georgia Institute of Technology, Atlanta, GA 30332, USA

²Astronomical Institute, Graduate School of Science, Tohoku University, Aoba, Sendai 980-8578, Japan

³National Astronomical Observatory of Japan, 2-21-1 Osawa, Mitaka, Tokyo 181-8588, Japan

ABSTRACT

The multiplicity of metal-free (Population III) stars may influence their feedback efficiency within their host dark matter halos, affecting subsequent metal enrichment and the transition to galaxy formation. Radiative feedback from massive stars can trigger nearby star formation in dense self-shielded clouds. In model radiation self-shielding, the H₂ column density must be accurately computed. In this study, we compare two local approximations based on the density gradient and Jeans length with a direct integration of column density along rays. After the primary massive star forms, we find that no secondary stars form for both the direct integration and density gradient approaches. The approximate method reduces the computation time by a factor of 2. The Jeans length approximation overestimates the H₂ column density by a factor of 10, leading to five numerically enhanced self-shielded, star-forming clumps. We conclude that the density gradient approximation is sufficiently accurate for larger volume galaxy simulations, although one must still caution that the approximation cannot fully reproduce the result of direct integration.

Key words: early universe: hydrodynamics — H II regions — ISM: molecules — methods: numerical — stars: formation — stars: Population III —

1 INTRODUCTION

The first generation of metal-free (Population III or Pop III) stars are crucial astronomical objects. Main-sequence Pop III stars emit copious amounts of ultraviolet (UV) photons, which can have either positive or negative effects on star formation. Ionizing photons with energies ≥ 13.6 eV can induce star formation in the interstellar medium (ISM) by enhancing the fraction of electrons, which catalyze formation reactions of hydrogen molecules (Ricotti, Gnedin, & Shull 2001; Johnson & Bromm 2006; Yoshida et al. 2007). Dissociating photons in the Lyman-Werner (LW) band (11.2–13.6 eV) can suppress star formation by destroying H₂ (Stacy et al. 2012; Hirano et al. 2015). Massive Pop III stars die with supernova (SN) events, which can also affect star formation (Klein, McKee, & Colella 1994; Nakamura et al. 2006; Chiaki et al. 2013; Magg et al. 2022). Sufficiently weak explosions can compress the surrounding gas and trigger star formation in a dense shell. Strong explosions can completely destroy ambient gas clumps and suppress star formation. Additionally, Pop III SNe supply the first elements heavier than lithium (metals) and their condensates (dust grains).

Additional cooling from metals and grains can lead the formation of first low-mass stars, by inducing the fragmentation of clouds (Omukai 2000; Schneider et al. 2003). The efficiency of radiation and SN feedback depends not only on the initial mass function (IMF) of Pop III stars but also on the number of Pop III stars per host dark matter minihalo (MH). Even with the state-of-the-art numerical simulations, it is challenging to predict the IMF and multiplicity within MHs.

Researchers have made valiant efforts to constrain the IMF of Pop III stars for the past two decades (Bromm et al. 1999; Abel et al. 2002; Yoshida et al. 2003). In metal-free collapsing clouds, hydrogen molecular cooling primarily induces fragmentation. H₂ cooling is inefficient at densities $\gtrsim 10^4$ cm⁻³, where local thermal equilibrium is established. The mass scale of fragments can be estimated to be the Jeans mass

$$M_J = 2 \times 10^3 M_\odot \left(\frac{\mu}{1.23} \right)^{-3/2} \left(\frac{n_H}{10^4 \text{ cm}^{-3}} \right)^{-1/2} \left(\frac{T}{200 \text{ K}} \right)^{3/2} \quad (1)$$

(Matsuda, Satō, & Takeda 1969). Multi-dimensional simulations showed that the Pop III stellar mass lies in a range of ~ 10 –1000 M_⊙ (Hirano et al. 2014; Susa et al. 2014).

The multiplicity of Pop III stars is also crucial for the

* E-mail: gen.chiaki@nao.ac.jp

efficiency of stellar feedback (Ritter et al. 2015). Recent numerical simulations have shown that, through the fragmentation of turbulent clouds or accretion discs, binaries and star clusters form at scales of $\sim 10\text{--}10^4$ AU (Turk et al. 2009; Greif et al. 2012; Susa 2019; Wollenberg et al. 2020). Sugimura et al. (2020) found that hierarchical binary/triplet systems form from an accretion disc $\sim 10^5$ yr after the formation of the primary protostar. The primary binary system consists of massive stars ($60\text{--}70 M_{\odot}$) with a separation of $\sim 10^4$ AU. One star hosts a small triplet system with moderately massive companions ($\sim 10 M_{\odot}$) at distances of $10^2\text{--}10^3$ AU.

In this paper, we focus on another channel of multiple Pop III star formation, so-called “triggered star formation” (Elmegreen & Lada 1977; Whitworth et al. 1994; Hosokawa & Inutsuka 2005, 2006). After the primary star forms in a MH, it emits ionizing photons if the star is sufficiently massive ($\gtrsim 10 M_{\odot}$). The overpressurized H II region and associated D-type ionization front drives a shock wave, creating a dense shell. It potentially can host star formation if the abundance of H_2 is sufficiently large ($y(\text{H}_2) \gtrsim 10^{-3}$) and becomes self-gravitating. The H_2 fraction in the D-type front can be reduced by LW photons emitted by the primary star. With a sufficiently large column density $N_{\text{H}_2} \gtrsim 10^{14} \text{ cm}^{-2}$ of hydrogen molecules, the self-shielding effect becomes important (Shull 1978; Federman, Glassgold, & Kwan 1979), where the dissociation rate k_{diss} is reduced by a shielding factor f_{sh} that is a non-linear function of N_{H_2} (Draine & Bertoldi 1996). Therefore, an accurate estimate of N_{H_2} is essential to model star formation, if any, in the D-type front.

It is ideal to calculate the column density by integrating the H_2 number density $n(\text{H}_2)$ from the source. Gas is generally optically thin in the LW band, and photons can propagate farther distance than ionizing photons. Radiation transport is especially difficult and computationally expensive in multi-dimensional simulations. To save the computational time, approximation methods are often used, where the column density is calculated using a typical length scale (shielding length) defined at each fluid element. Most researchers use the local Jeans length, which typically characterizes the size of a collapsing cloud. Another common choice is the length scale associated with the density or velocity gradient. The former characterizes the length scale of the density structure. The latter, so-called the Sobolev length, characterizes the length scale where a molecule cannot absorb redshifted photons (Sobolev 1960).

Several groups have studied the validity of the local approximation in various test problems. Hartwig et al. (2015) investigated the effect of H_2 self-shielding of background LW emission in the context of direct-collapse black hole formation. They found that the Jeans approach overestimates the LW intensity, compared to the direct integration. Safranek-Shrader et al. (2017) studied the self-shielding effects of H_2 and CO dissociation in a galactic disc. They compared direct ray-tracing and a variety of local approximations: the Jeans, Sobolev-length and density-gradient approach. They showed that the local approximation, especially the Jeans approach, in contrast with the findings of Hartwig et al. (2015), can reproduce the result of the full ray-tracing calculation well. In this work, we study the effect of the local approximation on the efficiency of triggered star formation, by comparing

the full ray-tracing calculation with the density gradient and Jeans length approaches.

Another important numerical parameter is the threshold density $n_{\text{H,th}}$ above which star formation is assumed to occur. Stars will form if the gas density grows up to $\gtrsim 10^{19} \text{ cm}^{-3}$ in a timescale shorter than the dynamical time (Greif et al. 2012). To resolve the gas dynamics in such dense regions, numerical timesteps are limited by the short Courant timescales ($\lesssim \text{yr}$). In Mpc-scale cosmological simulations of first-generations of stars and galaxies, several authors use $n_{\text{H,th}} = 10^5\text{--}10^7 \text{ cm}^{-3}$ (Smith et al. 2015; Schauer et al. 2021). Since the D-type front simultaneously contracts and expands with the thermal pressure from the inner H II region at comparable timescales, the density may only tentatively exceed the threshold value if $n_{\text{H,th}}$ is too small. In this work, we will test the convergence for $n_{\text{H,th}} = 10^6$ and 10^8 cm^{-3} .

We structure this paper as follows. In Section 2, we detail our cosmological hydrodynamics simulations and the relevant chemical processes. Then, we describe the results for the different schemes to estimate the H_2 column density and star formation density threshold in Section 3. In Section 4, we compare the computational cost for direct integration and local approximation. We also discuss the ramifications of the different schemes on star formation and feedback in the early Universe. Finally, we summarize the paper in Section 5.

Throughout the simulations, we adopt the cosmological parameters $\Omega_{\text{m}} = 0.3089$, $\Omega_{\text{CDM}} = 0.2603$, $\Omega_{\Lambda} = 0.6911$, and $H_0 = 67.74 \text{ km s}^{-1} \text{ Mpc}^{-1}$ (Planck Collaboration et al. 2016). We run the simulations in comoving coordinates, but we describe physical quantities in proper coordinates throughout this paper, unless otherwise specified. We use the mass fraction of hydrogen nuclei $X_{\text{H}} = 0.76$. All the figures in this paper are created with the YT toolkit (Turk et al. 2011).¹

2 METHOD

2.1 Cosmological simulation

We run a suite of cosmological simulations with the adaptive mesh refinement (AMR)/ N -body simulation code ENZO (Bryan et al. 2014; Brummel-Smith et al. 2019). We solve the hydrodynamics equations with the piecewise parabolic method (PPM) in an Eulerian frame (Woodward & Colella 1984; Bryan et al. 1995), using a Harten-Lax-van Leer-Contact (HLLC) Riemann solver to accurately capture hydrodynamical shocks and compute advection of chemical species across contact discontinuities. We follow the DM dynamics with an N -body particle-mesh solver (Efstathiou et al. 1985; Bryan & Norman 1997).

Computational cells are progressively refined by a factor of two in space when satisfying the following criteria:

- (a) The baryon mass in a cell exceeds $3m_{\text{b},0} \times 2^{-0.2L}$ on a refinement level L , where $m_{\text{b},0}$ is the mean baryon mass on the root grid.

¹ <https://yt-project.org/>.

Table 1. Initial parameters of each run

 (a) Threshold density $n_{\text{H,th}}$ for star formation.

ENZO parameter	n6	n8	Note
PopIIIOverDensityThreshold	-1e6	-1e8	Minimum density for star formation. ^a

(b) Approximation methods for LW transfer.

ENZO parameter	TestA	TestB	TestC	Note
RadiativeTransferOpticallyThinH2	0	1	1	Flag to use local approximation.
RadiativeTransferUseH2Shielding	1	—	—	Flag to calculate the self-shielding function.

GRACKLE parameter	TestA	TestB	TestC	Note
H2.self_shielding	—	1	3	Types of local approximation method. ^b

 Note — (a) If a negative value is assigned, ENZO uses its absolute value in units of cm^{-3} .

(b) 1: Density gradient. 2: User-supplied length-scale. 3: Jeans length.

(b) The DM particle mass contained by a cell exceeds $3m_{\text{dm},0}$, where $m_{\text{dm},0}$ is the mean DM mass on the root grid.

(c) The local Jeans length λ_{J} is resolved less than 64 cells.

The negative coefficient -0.2 in the exponent of criterion (a) invokes the super-Lagrangian refinement for the gas component while criterion (b) ensures Lagrangian refinement for the DM. When the baryon density starts to increase in the run-away collapse phase, cells are refined mostly on criterion (c). This criterion warrants that the local Jeans length is resolved sufficiently to prevent spurious fragmentation (Trulove et al. 1997; Turk et al. 2012).

We generate the initial conditions in a periodic box with a side length of $1h^{-1}$ Mpc (comoving) with MUSIC (Hahn & Abel 2011). We initially run a DM-only simulation with a base resolution 512^3 and identify the most massive halo with a mass $5.97 \times 10^8 M_{\odot}$ at redshift $z = 7$ with a halo-finding code ROCKSTAR (Behroozi, Wechsler, & Wu 2013). After initially refining the halo Lagrangian region with two additional AMR levels, i.e., with higher spatial resolution by a factor of four, we restart the simulation adding the baryon component. With this zoom-in strategy, the effective resolution is 2048^3 , and the minimum DM particle mass is $12.4 M_{\odot}$.

2.2 Pop III star formation

The main coolant of a primordial cloud is molecular hydrogen. To calculate the fraction and cooling rate of H_2 , we model the non-equilibrium chemistry with the chemistry/cooling library GRACKLE (Smith et al. 2017; Chiaki & Wise 2019).² We solve a chemical network of 15 primordial species, e^- , H^+ , H , H^- , H_2^+ , H_2 , D^+ , D , D^- , HD^+ , HD , He^+ , He^{2+} and HeH^+ . This chemical network includes the collisional ionization/recombination of H/He and formation/dissociation of H_2/HD molecules. We compute the rates of radiative cooling including inverse Compton cooling, bremsstrahlung, H/He transition line cooling, H_2 rovibrational transition line cooling and HD vibrational transition line cooling. We also consider chemical heating from H_2

formation, where the binding energy (4.48 eV per molecule) is converted to the thermal energy (see Omukai 2000).

When certain criteria with a molecular cloud are met, we assume that a Pop III star forms. In reality, a star forms after gas is accreted onto a protostellar hydrostatic core with a density of $n_{\text{H}} \sim 10^{19} \text{cm}^{-3}$ (Larson 1969; Greif et al. 2012). In this work, to save the computational cost, we insert a Pop III star particle in cells that satisfy the following criteria:

- (i) the gas density exceeds a threshold density $n_{\text{H,th}}$,
- (ii) the gas flow is convergent, $\nabla \cdot \mathbf{v} < 0$,
- (iii) the cooling time is less than the dynamical time,
- (iv) the H_2 fraction exceeds a threshold value, $y_{\text{th}}(\text{H}_2) = 10^{-3}$.

We assign the mass M_{PopIII} of the star particle, randomly sampling from a Larson-type IMF

$$\frac{dN}{d \log M_{\text{PopIII}}} \propto M_{\text{PopIII}}^{-1.3} \exp \left[- \left(\frac{M_{\text{char}}}{M_{\text{PopIII}}} \right)^{1.6} \right], \quad (2)$$

where M_{char} is a characteristic mass of Pop III stars. We set the minimum, maximum and characteristic mass to 1, 300 and $20 M_{\odot}$, respectively. With our random seed, the mass of the primary star is $10.4 M_{\odot}$.

2.3 Radiation feedback from a Pop III star

During the main sequence of a Pop III star, we solve the radiative transfer equation with the adaptive ray tracing module MORAY (Wise & Abel 2011). We calculate the number flux P of ionizing/dissociating photons passing through each computational cell. From each radiation source, we integrate P along rays in directions based on HEALPIX (Hierarchical Equal Area isoLatitude Pixelation; Górski et al. 2005). The number of rays is 12×4^l with a level l . The initial level (RadiativeTransferInitialHEALPixLevel) is set to 1, and rays are adaptively split as they travel away from the source. We set the minimum number of rays passing through a cell (RadiativeTransferRaysPerCell) to 5.1.

We divide the spectral energy distribution of the source into four energy bins of (E_{LW} , E_{H} , E_{He} , E_{He^+}) = (12.8, 28.0, 30.0, 58.0) eV, corresponding to the dissociating, H, He and He^+ ionizing photons, respectively. The

² <https://grackle.readthedocs.io/>.

Table 2. Properties of forming Pop III stars

$n_{\text{H,th}}$ [cm ⁻³]	Test	t_{form} [kyr]	D [pc]	M_{PopIII} [M _⊙]	t_{life} [Myr]	$Q(\text{H})$ [s ⁻¹]	$Q(\text{He})$ [s ⁻¹]	$Q(\text{He}^+)$ [s ⁻¹]	$Q(\text{LW})$ [s ⁻¹]
10 ⁶	A	0.0	0.0	10.4	16.9	5.42×10^{47}	1.78×10^{47}	2.84×10^{41}	7.96×10^{47}
	B	0.0	0.0	10.4	16.9	5.42×10^{47}	1.78×10^{47}	2.84×10^{41}	7.96×10^{47}
	C	0.0	0.0	10.4	16.9	5.42×10^{47}	1.78×10^{47}	2.84×10^{41}	7.96×10^{47}
	⋮	20.6	0.143	16.0	9.6	2.04×10^{48}	7.95×10^{47}	2.36×10^{43}	2.78×10^{48}
	⋮	30.7	0.301	28.7	5.4	9.77×10^{48}	4.56×10^{48}	3.54×10^{45}	1.22×10^{49}
	⋮	40.6	0.734	28.1	5.5	9.23×10^{48}	4.29×10^{48}	2.97×10^{45}	1.15×10^{49}
	⋮	53.9	0.336	33.3	4.8	1.40×10^{49}	6.79×10^{48}	1.07×10^{46}	1.71×10^{49}
⋮	63.8	0.435	18.8	8.0	3.21×10^{48}	1.32×10^{48}	1.04×10^{44}	4.26×10^{48}	
10 ⁸	A	0.0	0.0	10.4	16.9	5.42×10^{47}	1.78×10^{47}	2.84×10^{41}	7.96×10^{47}
	B	0.0	0.0	10.4	16.9	5.42×10^{47}	1.78×10^{47}	2.84×10^{41}	7.96×10^{47}
	C	0.0	0.0	10.4	16.9	5.42×10^{47}	1.78×10^{47}	2.84×10^{41}	7.96×10^{47}
	⋮	37.1	0.0418	16.0	9.6	2.04×10^{48}	7.95×10^{47}	2.36×10^{43}	2.78×10^{48}
	⋮	62.2	0.0390	67.6	3.1	6.27×10^{49}	3.47×10^{49}	8.27×10^{47}	7.10×10^{49}

Note — (1) threshold density for star formation. (2) ID of tests. (3) formation time. (4) distance from the primary star. (5) mass. (6) lifetime. (7–10) emission rates of H, He and He⁺ ionizing photons and H₂ dissociating photons.

energies are fixed regardless of the stellar mass for simplicity. We use the fits from [Schaerer \(2002\)](#) to calculate the emission rates of dissociating and H, He, and He⁺ ionizing photons, $Q(\text{LW})$, $Q(\text{H})$, $Q(\text{He})$ and $Q(\text{He}^+)$, respectively, as a function of stellar mass.

For ionizing photons, we solve the radiative transfer equation for all runs. We calculate the optical depth along a ray segment passing through a cell with a size dr as

$$d\tau_i = \sigma_i n_i dr, \quad (4)$$

where σ_i and n_i is the absorption cross-section (taken from [Verner et al. 1996](#)) and number density of a species $i = \{\text{H}, \text{He}, \text{He}^+\}$, respectively. The photon flux is reduced by

$$dP_{\text{ion},i} = P_{\text{ion},i}(1 - e^{-d\tau_i}) \quad (4)$$

across the ray segment. Then we calculate the photoionization rate as

$$k_{\text{ion},i} = \frac{dP_{\text{ion},i}}{n_i V_{\text{cell}} dt_P} \quad (5)$$

during a photon integration timestep dt_P , where V_{cell} is a cell volume, from a single ray. The total photoionization rate is the sum of all the rays passing through the cell.

To calculate the photodissociation rate, we test the following three methods.

TestA Direct integration of H₂ number density

In this test, we compute the H₂ dissociation rate k_{diss} using the number of LW photons P_{LW} entering a computational cell as

$$k_{\text{diss}} = \sum_{\text{rays}} \frac{P_{\text{LW}} \sigma_{\text{H}_2} \Omega_{\text{ray}} r^2 dr}{A_{\text{cell}} V_{\text{cell}} dt_P}, \quad (6)$$

where A_{cell} is the face area of the computational cell, r is a distance between the source and the cell, Ω_{ray} is the solid angle of a HEALPIX cell. We use a reaction cross-section $\sigma_{\text{H}_2} = 3.71 \times 10^{-18}$ cm² of H₂ ([Abel et al. 1997](#)). In the cell, photons are attenuated as

$$dP_{\text{LW}} = P_{\text{LW}} [f_{\text{sh}}(N_{\text{H}_2} + dN_{\text{H}_2}) - f_{\text{sh}}(N_{\text{H}_2})], \quad (7)$$

where $f_{\text{sh}}(N_{\text{H}_2})$ is a shielding function. We use the fitting function

$$f_{\text{sh}}(N_{\text{H}_2}) = \frac{0.965}{(1 + x/v_{\text{th},5})^2} + \frac{0.035}{(1 + x)^{0.5}} \times \exp[-8.5 \times 10^4 (1 + x)^{0.5}] \quad (8)$$

([Wolcott-Green, Haiman, & Bryan 2011](#)), by setting the parameter `RadiativeTransferH2ShieldType = 1`, where $x = N_{\text{H}_2}/5 \times 10^{14}$ cm⁻² and $v_{\text{th},5} = v_{\text{th}}/10^5$ cm s⁻¹. The column density is directly integrated as

$$N_{\text{H}_2} = \int n(\text{H}_2) ds \quad (9)$$

along a HEALPIX ray s .

TestB Local approximation with the density gradient

In local approximations, the dissociation rate is estimated as

$$k_{\text{diss}} = f_{\text{sh}}(N_{\text{H}_2}) \frac{Q(\text{LW}) \sigma_{\text{H}_2}}{4\pi r^2} \quad (10)$$

using the functional form $f_{\text{sh}}(N_{\text{H}_2})$ given in Eq. (8). We compute the column density as

$$N_{\text{H}_2} = n(\text{H}_2) l_{\text{sh}} \quad (11)$$

with a length scale l_{sh} (shielding length) defined with physical quantities of each fluid element. In **TestB**, we estimate l_{sh} as the density gradient

$$l_{\text{sh},D} = \frac{\rho}{|\nabla \rho|}, \quad (12)$$

where ρ is the density of a cell.

TestC Local approximation with the Jeans length

In this test, we use the same local approximation as **TestB** (Eq. 11), but the shielding length is calculated from the local Jeans length

$$l_{\text{sh},J} \equiv \lambda_J = \left(\frac{\pi c_s^2}{G\rho} \right)^{1/2}, \quad (13)$$

where c_s is the sound speed of a cell.

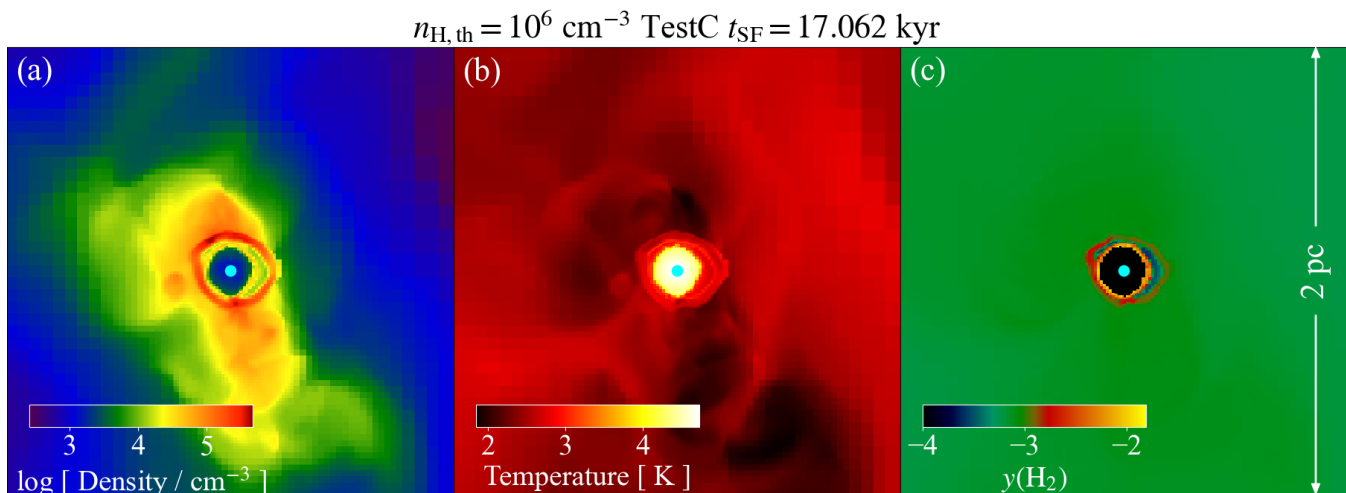


Figure 1. Slices of (a) density, (b) temperature and (c) number fraction $y(\text{H}_2)$ of hydrogen molecules relative to hydrogen nuclei for **TestC** at the time 17.1 kyr after the primary star formation and just before the secondary star formation. The plotted window is centered at the position of the primary Pop III star (cyan circle) with a side length of 2 pc on the computational x - y plane.

2.4 Star formation density threshold

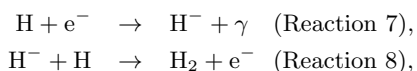
The threshold density $n_{\text{H,th}}$ can affect the efficiency of Pop III star formation. We compare two cases with $n_{\text{H,th}} = 10^6$ and 10^8 cm^{-3} , hereafter called **n6** and **n8**, respectively. The former value is often used in small-volume cosmological simulations of the first galaxies (Skinner & Wise 2020; Schauer et al. 2021) and lower values in larger-volume simulations (Wise et al. 2012; Xu et al. 2016; Jeon, Besla, & Bromm 2021). In this paper, we mainly show the result for **n6** as a fiducial case. We run simulations of **TestA**, **B** and **C** for each $n_{\text{H,th}}$, and Table 1 summarizes the initial parameters in the six runs.

We terminate our simulations 0.1 Myr after the formation of the primary star, that is shorter than the lifetime ($\sim 10 \text{ Myr}$) of a star with a mass $\sim 10 M_{\odot}$. We confirm that the number of Pop III stars is unchanged by running the simulation for **TestB** until the lifetime of the primary star. We output snapshots at every 5000 yr to analyze the star formation history. Hereafter, we measure the time t_{SF} from the primary star formation.

3 RESULTS

3.1 Number of forming Pop III stars

In this section, we present the results for case **n6**, where the threshold density $n_{\text{H,th}}$ for star formation is 10^6 cm^{-3} . At a redshift of $z = 25.1$ in a MH with a virial mass of $3.39 \times 10^5 M_{\odot}$ and virial radius of 86.8 pc, H_2 molecules form through the reactions



catalyzed by free electrons (H^- -process; Peebles 1980). The gas temperature decreases below $\sim 1000 \text{ K}$ through rovibrational cooling of H_2 . A cloud collapses in a runaway manner. When the density reaches 10^6 cm^{-3} , we insert the primary Pop III star. With our random seed, the

mass of the primary star is assigned to $10.4 M_{\odot}$. Its lifetime is $t_{\text{life}} = 16.9 \text{ Myr}$, and the photon emission rates are $(Q(\text{LW}), Q(\text{H}), Q(\text{He}), Q(\text{He}^+)) = (5.42 \times 10^{47}, 1.78 \times 10^{47}, 2.84 \times 10^{41}, 7.96 \times 10^{47}) \text{ s}^{-1}$. An H II region forms around the star through the absorption of ionizing photons, and modifies the density structure in the ISM. Photons in the LW band dissociate H_2 molecules and affect the formation of any secondary star.

The subsequent star formation history varies for different local approximation methods. Table 2 summarizes the properties of Pop III stars forming during the first 0.1 Myr after the primary star forms. Only one Pop III star forms for **TestA** and **B**, while six stars form for **TestC**. In **TestC**, the secondary stars with (random) masses $20\text{--}30 M_{\odot}$ form at distances $D = 0.1\text{--}0.7 \text{ pc}$ from the primary star at the time $t_{\text{SF}} = 20\text{--}60 \text{ kyr}$. Compared to **TestA**, the number of Pop III stars is consistent for **TestB** and overestimated for **TestC**.

In the following subsections, we describe the evolution of the H II region for **TestA** and **B** (Section 3.2) and interpret the secondary star formation in case **TestC** (Section 3.3). Then, we describe the result for **n8** in Section 3.4.

3.2 Evolution of H II regions

Fig. 1 shows the slices of density, temperature and the number fraction $y(\text{H}_2)$ of H_2 to hydrogen nuclei at $t_{\text{SF}} = 17.1 \text{ kyr}$, just before the secondary star formation for **TestC**. In this figure, we plot the results only for **TestC**. The distribution of density and temperature for **TestA** and **B** is almost the same as **TestC**, but $y(\text{H}_2)$ is smaller than for the two other tests by eight orders of magnitude in the dense shell outside the H II region.

Fig. 2 shows the density, temperature, e^- and H_2 fraction, column density and photodissociation rate along a ray from the source to the density maximum. The UV photons with energies $E \geq 13.6 \text{ eV}$ emitted by the primary star ionizes the adjacent gas. The temperature increases to $\sim 5 \times 10^4$

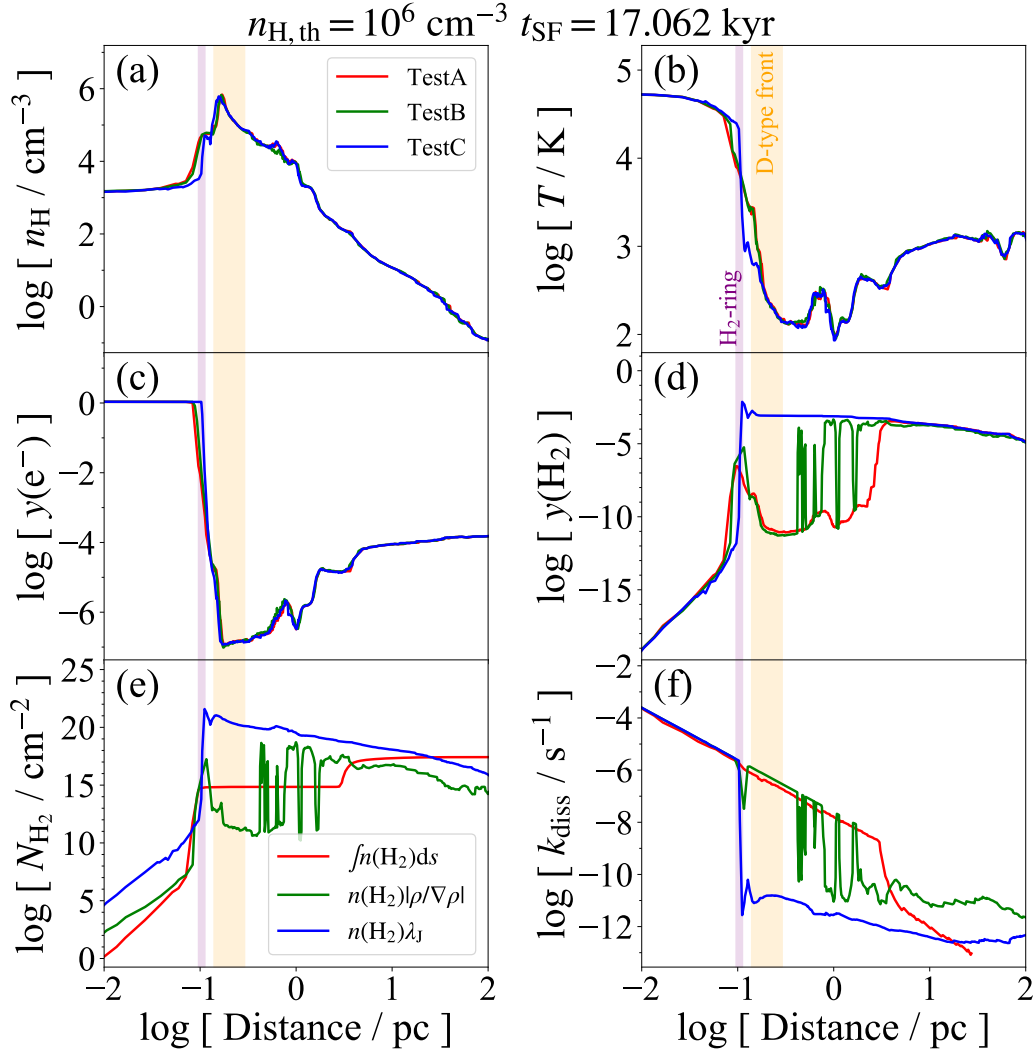


Figure 2. (a) Density n_{H} , (b) temperature T , (c) e^- fraction $y(e^-)$ (solid curves), H^- fraction $y(\text{H}^-)$ (dashed curves), (d) H_2 fraction $y(\text{H}_2)$, (e) H_2 column density N_{H_2} and (f) dissociation rate k_{diss} as a function of distance from the primary Pop III star on a ray from the source to the density maximum at the time 17.1 kyr after the primary star formation. The red, green and blue curves denote the results for **TestA**, **TestB** and **TestC**, respectively. The purple and orange shaded regions represent the H_2 -ring and D-type front for **TestA**, respectively.

K, comparable to the surface temperature of the star. Due to the strong thermal pressure ($\sim 10^{-9} \text{ dyn/cm}^2$), the density declines to $\sim 400 \text{ cm}^{-3}$ in the ionized region. Just outside the ionizing front (I-front), a dense shell (D-type front) forms. We define the D-type front as the region with densities above 0.1 times the maximum density (orange shaded region in Fig. 2). In the region between the I-front and D-type front, the gas is partly ionized with an electron fraction of $y(e) \sim 10^{-3}$. The H_2 fraction increases through the H^- -process (Reactions 7 and 8), and a so-called “ H_2 -ring” appears (Fig. 1c). We define the H_2 -ring as the region with H_2 fractions above 0.1 times the maximum, $y_{\text{max}}(\text{H}_2) \sim 10^{-7}$ (purple shaded region in Fig. 2). In Fig. 2, we plot the D-type front and H_2 -ring for **Test A**, but their positions are almost the same for the other tests.

At the time $t_{\text{SF}} = 17.1 \text{ kyr}$, the radius of the D-type front reaches $\sim 0.1 \text{ pc}$ (Fig. 2). The gas flow is convergent, and the density increases up to $\sim 10^6 \text{ cm}^{-3}$, comparable

to $n_{\text{H,th}}$. Therefore, the D-type front naturally satisfies the criteria (i) and (ii) for star formation. If H_2 fraction is larger than $y_{\text{th}}(\text{H}_2)$, the criteria (iii) and (iv) will be also satisfied. For **TestA** and **B**, due to ineffective shielding, a sufficient fraction of dissociating photons can penetrate into the D-type front, and the formation of secondary stars is prevented. We discuss the result in a quantitative manner in subsequent sections.

(a) **TestA**

For **TestA**, the density reaches the maximum value of $n_{\text{H,max}} = 6.88 \times 10^5 \text{ cm}^{-3}$ in the D-type front at a distance 0.170 pc at the time $t_{\text{SF}} = 17.1 \text{ kyr}$. Since $n_{\text{H,max}}$ is comparable to $n_{\text{H,th}}$, the criteria (i) and (ii) will be satisfied if the convergence continues. Just inside the D-type front, the H_2 ring forms at a distance 0.0960 pc, where the fraction of H_2 reaches only up to $y(\text{H}_2) = 2.95 \times 10^{-7}$. The column density increases rapidly in the H_2 ring, and

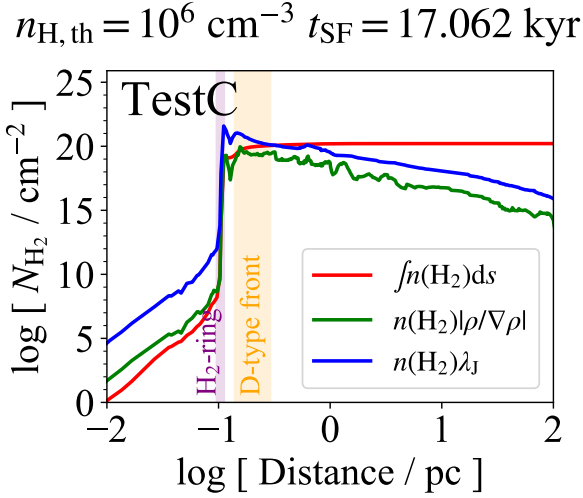


Figure 3. H_2 column density calculated with different schemes as a function of distance from the primary Pop III star on a ray from the source to the density maximum at the time 17.1 kyr after the primary star formation. From the snapshot of **TestC**, we calculate the column density by integrating H_2 density along the ray (red curve) and using density gradient $|\rho/\nabla\rho|$ (green curve). The blue curve is the same as the one in Fig. 2e. The purple and orange shaded regions represent the H_2 -ring and D-type front, respectively, the same as Fig. 2.

it reaches a plateau of $N_{\text{H}_2} \sim 7 \times 10^{14} \text{ cm}^{-3}$ (red curves in Fig. 2). At the density maximum, the column density is $N_{\text{H}_2} = 6.98 \times 10^{14} \text{ cm}^{-2}$. With the temperature 856 K, the shielding fraction is $f_{\text{sh}} = 0.704$ (Eq. 8), that is, dissociation photons are only marginally shielded in the H_2 -ring. Since H_2 molecules cannot avoid dissociation, the H_2 fraction declines down to $y(\text{H}_2) \sim 10^{-10}$. The star-formation criteria (iii) and (iv) are not satisfied, and thus secondary stars do not form.

(b) **TestB**

For **TestB**, only one Pop III star forms during the simulation, which is the same result as **TestA**. However, this does not necessarily mean that the Sobolev-like approximation can reproduce the result of direct integration. The D-type front is a potential star forming site, because its density ($6.74 \times 10^5 \text{ cm}^{-3}$) is comparable to $n_{\text{H},\text{th}}$ at $t_{\text{SF}} = 17.1$ kyr. The shielding length $l_{\text{sh},\text{D}} = 0.111 \text{ pc}$ at the density maximum characterizes the length scale of the D-type front (0.139 pc). The column density is estimated as the product of H_2 fraction at the density maximum and the thickness of the D-type front. As we have discussed in the previous section, the H_2 -ring mostly contributes to the column density at the density maximum for **TestA**. This indicates that the local approximation fails to capture the contribution of the spatially separated region. The column density is indeed underestimated to be $N_{\text{H}_2} = 2.95 \times 10^{13} \text{ cm}^{-2}$, compared to the value $6.98 \times 10^{14} \text{ cm}^{-2}$ for **TestA** by a factor of 20, because the H_2 fraction is smaller in the D-type front than in the H_2 -ring. Nevertheless, since the shielding factor $f_{\text{sh}}(N_{\text{H}_2})$ is insensitive to N_{H_2} at $N_{\text{H}_2} \lesssim 5 \times 10^{14} \text{ cm}^{-3}$, $f_{\text{sh}} = 0.982$ is comparable to the value for **TestA**. Consequently, secondary stars do not form as for **TestA**.

3.3 Secondary star formation for **TestC**

For **TestC**, the shielding factor is overestimated, compared to **TestA**, that consequently overproduces Pop III stars. At $t_{\text{SF}} = 17.1$ kyr, just before the formation of the first secondary star, the dissociation rate $k_{\text{diss}} = 8.48 \times 10^{-12} \text{ s}^{-1}$ is much smaller than for **TestA** and **B** at the density maximum. A large fraction (9.67×10^{-4}) of H_2 survives, and $y(\text{H}_2)$ exceeds the threshold value 10^{-3} at $t_{\text{SF}} = 20.6$ kyr. Feedback from the secondary stars further induces repetitive star formation. By $t_{\text{SF}} = 0.1$ Myr, six Pop III stars form.

This behavior occurs because the Jeans length approach overestimates the H_2 column density. For a fair comparison, we calculate N_{H_2} with the three different methods from a snapshot for **TestC** at the time $t_{\text{SF}} = 17.1$ kyr (Fig. 3). The blue and green curves show the result for the direct integration and the density gradient approach, respectively. The Jeans length approach overestimates $N_{\text{H}_2} = 9.45 \times 10^{20} \text{ cm}^{-2}$ at the density maximum, compared to 4.87×10^{19} and $9.19 \times 10^{19} \text{ cm}^{-2}$ for direct integration and density gradient approach by a factor of two and ten, respectively. Since the Jeans length originally characterizes the length scale of a quasi-static collapsing cloud, it is larger than the length scale of the D-type front contracting with the thermal pressure of the H II region. The shielding factor $f_{\text{sh}} = 8.36 \times 10^{-6}$ is smaller than the direct integration method, because $f_{\text{sh}}(N_{\text{H}_2})$ is a decreasing function of N_{H_2} for $N_{\text{H}_2} \gtrsim 5 \times 10^{14} \text{ cm}^{-3}$ (Eq. 8). Dissociating photons cannot penetrate into the D-type front due to the high efficiency of self-shielding, and thus the H_2 fraction exceeds the critical value. After this point, secondary stars form in the D-type front.

3.4 Effect of the threshold density for star formation

In this section, we describe the results for a higher threshold density $n_{\text{H},\text{th}} = 10^8 \text{ cm}^{-3}$ (n8). The primary star forms at a redshift 25.0, 0.3 Myr later than n6. The stellar UV photons create an H II region, and a D-type front forms just outside a H_2 -ring like the n6 case. As Table 2 summarizes, only one Pop III star forms in **TestA** and **B**, while three stars form in **TestC** when we terminate the simulations at the time $t_{\text{SF}} = 0.1$ Myr. For **TestC**, the number of Pop III stars becomes smaller than case n6 and approaches the value for **TestA**. However, the result still does not converge even for the high $n_{\text{H},\text{th}} = 10^8 \text{ cm}^{-3}$.

Fig. 4 shows density, temperature, e^- and H_2 fraction, H_2 column density and dissociation rate along a ray from the primary star to the density maximum at $t_{\text{SF}} = 36.7$ kyr, just before the secondary star formation for **TestC**. For **TestA**, the column density increases only up to $1.43 \times 10^{13} \text{ cm}^{-2}$ in the H_2 -ring at a distance $6.29 \times 10^{-3} \text{ pc}$. The H_2 -ring is optically thin ($f_{\text{sh}} = 0.987$), and almost all LW photons enter the D-type front at a distance 0.0308 pc (red vertical line in Fig. 4). The H_2 fraction is 7.22×10^{-12} , well below the threshold for star formation.

For **TestB**, the shielding length is $l_{\text{sh},\text{D}} = 0.151 \text{ pc}$, and $N_{\text{H}_2} = 4.68 \times 10^{16} \text{ cm}^{-3}$ at the density maximum (green dotted line in Fig. 4). The corresponding shielding factor is small (0.0192), but N_{H_2} just increases temporarily. Around the density maximum, we can see spikes in N_{H_2} with a height

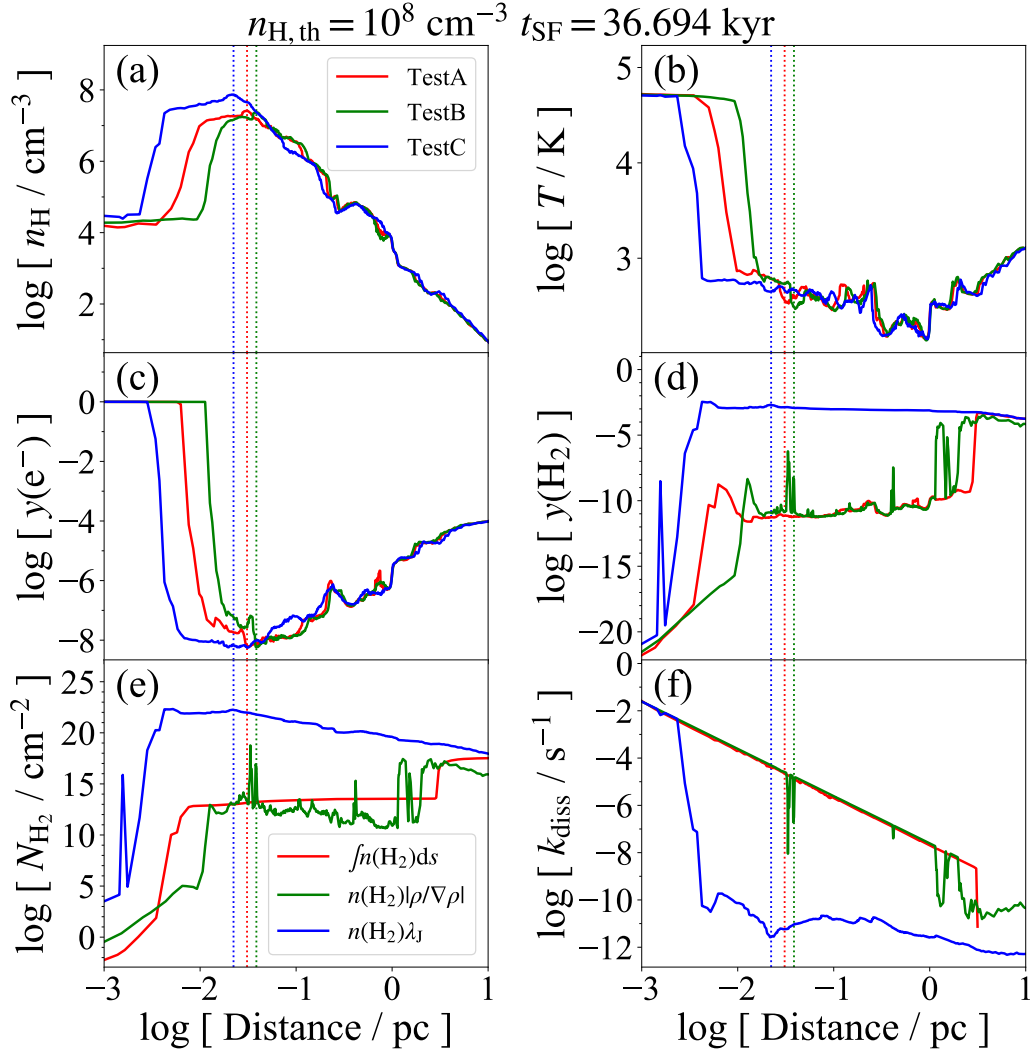


Figure 4. Same as Fig. 2 but at the time 36.7 kyr after the primary Pop III star formation just before the secondary star formation for **TestC** for the threshold density $n_{\text{H,th}} = 10^8 \text{ cm}^{-3}$ for star formation. The vertical dotted lines show the distance of the density maxima. The red, green and blue curves indicate the results for **TestA**, **TestB** and **TestC**, respectively.

of six orders of magnitude and a width of $\sim 3 \times 10^{-3}$ pc (green curve in Fig. 4e). The sound crossing time of the spikes is $t_{\text{sc}} \sim 1$ kyr for the temperature 300 K, shorter than the dynamical time ~ 10 kyr. This indicates that the spikes are dumped very quickly. The small-scale noise is generated by the sensitivity of the length $l_{\text{sh,D}}$ to the turbulent motion (convergent flow) of the gas. In the D-type front, the column density is $\sim 10^{13} \text{ cm}^{-2}$ on average, which corresponds to $f_{\text{sh}} \sim 1$. Therefore, nearly all of the H_2 molecules are destroyed by LW photons, and further star formation does not occur in the D-type front.

For **TestC**, the shielding length is $l_{\text{sh,J}} = 0.0392$ pc, and the column density is $N_{\text{H}_2} = 1.74 \times 10^{22} \text{ cm}^{-2}$. As in Section 3.3, we compare column densities calculated with the three different methods, using a snapshot for **TestC** at the time $t_{\text{SF}} = 36.7$ kyr (Fig. 5). The column density is overestimated with respect to $4.12 \times 10^{21} \text{ cm}^{-2}$ for the direct integration by a factor of four. The shielding factor is $f_{\text{sh}} = 5.44 \times 10^{-8}$, and k_{diss} in the D-type front is small ($2.70 \times 10^{-12} \text{ s}^{-1}$). As

a result, the criterion for star formation is satisfied, and the secondary stars form in this test.

4 DISCUSSION

4.1 Computational time

We carry out the simulations with 448 cores on the Frontera supercomputer system at Texas Advanced Computing Center. Table 3 shows the computational time t_{comp} for the different approximate methods and threshold densities $n_{\text{H,th}}$. The computational time is generally longer for **n8** than for **n6** by a factor of ~ 10 . Because the gas density increases up to 10^8 cm^{-3} in **n8**, it takes additional computation to solve hydrodynamics, chemistry and radiative transfer in the region with densities $\sim 10^6 < n_{\text{H}} / \text{cm}^{-3} < 10^8$.

For **n6**, t_{comp} is shorter at 6.35 hours for **TestB** than the 15.5 hours taken for **TestA** by a factor of 2.5. The local approximation can reduce the numerical cost, compared to

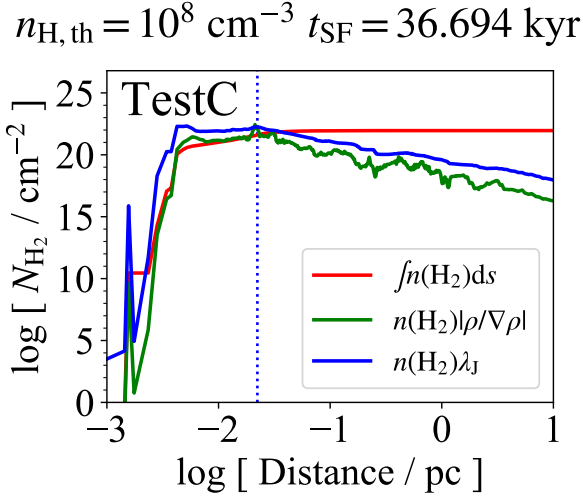


Figure 5. The same as Fig. 3 but at the time 36.7 kyr after the primary Pop III star formation just before the secondary star formation for **TestC** for the threshold density $n_{\text{H,th}} = 10^8 \text{ cm}^{-3}$ for star formation. The vertical dotted line shows the distance of the density maximum.

solving the radiative transfer equation of LW photons. We estimate the fraction f_{RT} of computational time for radiative transfer calculation that includes the ionizing photons and, for **TestA**, the LW photons (fourth column of Table 3). For **TestB**, $f_{\text{RT}} = 46.1\%$, smaller than 86.9% for **TestA**. For **TestC**, t_{comp} is similar to **TestA**.

In Mpc-scale cosmological simulations, hundreds of Pop III stars form by a redshift ~ 10 (Skinner & Wise 2020; Jeon, Besla, & Bromm 2021; Schauer et al. 2021). It is costly to solve the radiative transfer equation of LW photons for all the stars, because LW photons reach longer distance than ionizing photons by two orders of magnitude (see Fig. 2). The density gradient approach can reduce the computational time by a factor of 2.5, reproducing the star formation history although it fails to include the contribution of the H_2 -ring to the column density and thus underestimates the column density.

4.2 Feedback effects

We have studied that the approximation methods of LW radiative transfer and their effects on the multiplicity of Pop III stars in a MH. This may significantly affect the efficiency of radiative and SN feedback. In this section, we discuss the impact from the different numerical setups in a quantitative manner.

4.2.1 Ionization feedback

The emission rates of UV photons is roughly proportional to the number of massive Pop III stars. In Fig. 6a, we compare the radial profiles of the H^+ and He^+ abundances at the time $t_{\text{SF}} = 0.1 \text{ Myr}$ for the three approximation methods for **n6**. We define the radius of the I-front as the distance where $y(\text{H}^+) = 0.01$, which is comparable to the radius of the I-front for He. The I-front reaches 31.3 comoving pc

Table 3. Computational time for each run

$n_{\text{H,th}}$ [cm^{-3}]	Test	t_{comp} [hours]	f_{RT} [%]
10^6	A	15.5	86.7
	B	6.35	46.1
	C	16.4	36.9
10^8	A	143	86.9
	B	65.1	24.8
	C	59.9	48.0

Note — t_{comp} : Computational time in units of hour. f_{RT} : Fraction of computational time for radiative transfer. We carry out these simulations with 448 cores on the supercomputer system TACC/Frontera.

for **TestC**, which is larger than $\sim 5 \text{ pc}$ for the other runs, because multiple radiation sources form.

In this work, we terminate the simulations at $t_{\text{SF}} = 0.1 \text{ Myr}$, but we can predict whether the H II region will eventually expand beyond the virial radius. Chiaki et al. (2018) estimated the critical halo mass, below which the radiation energy exceeds the binding energy of a MH, to be

$$M_{\text{halo,cr}} = 5.64 \times 10^6 M_{\odot} \left(\frac{v_{\text{D}}}{10 \text{ km s}^{-1}} \right)^{3/4} \left(\frac{t_{\text{lifc}}}{10 \text{ Myr}} \right)^{3/4} \times \left(\frac{Q(\text{H})}{5 \times 10^{49} \text{ s}^{-1}} \right)^{3/4} \left(\frac{1+z}{26} \right)^{-3/2}, \quad (14)$$

where v_{D} is the expansion velocity of a D-type front, and t_{lifc} is the stellar lifetime. A Pop III star with a mass $10.4 M_{\odot}$ emits ionizing photons at a rate $5.42 \times 10^{47} \text{ s}^{-1}$ (Table 2). In models where a single star forms (**TestA** and **B**), the critical halo mass is $1.89 \times 10^5 M_{\odot}$. Since the mass of the host halo $3.39 \times 10^5 M_{\odot}$ exceeds the critical mass, we can predict that the H II region does not expand beyond the virial radius. For **TestC**, the total emission rate is 3.88×10^{49} and $6.53 \times 10^{49} \text{ s}^{-1}$ for **n6** and **n8**, respectively. Since the halo mass is below the critical mass (4.66×10^6 and $6.89 \times 10^6 M_{\odot}$, respectively), we can predict that ionization photons can reach IGM. This indicates that the different models can affect the initial stage of cosmic reionization.

4.2.2 LW feedback

LW radiation can suppress star formation in neighboring clouds by dissociating H_2 (O’Shea & Norman 2008; Hirano et al. 2015) or sometimes trigger the formation of supermassive stars and black holes (Omukai 2001; Wise et al. 2019; Regan et al. 2020). We compare the LW intensity

$$J_{\text{LW}} = \frac{f_{\text{sh}} E_{\text{LW}} Q(\text{LW})}{4\pi \Delta\nu_{\text{LW}} 4\pi D^2}, \quad (15)$$

where D is the distance from a star (cluster), and $\Delta\nu_{\text{LW}} = 5.80 \times 10^{14} \text{ Hz}$ is the width of the LW band. Hereafter we use the LW intensity J_{21} in units of $10^{-21} \text{ erg s}^{-1} \text{ cm}^{-2} \text{ Hz}^{-1} \text{ sr}^{-1}$.

Fig. 6b shows the LW intensity as a function of the distance from the primary star at the time $t_{\text{SF}} = 0.1 \text{ Myr}$. At distances $D \lesssim 0.01 \text{ kpc}$ (comoving), the intensity is largest for **TestC** because of multiple Pop III star formation. At $0.01 \lesssim D/\text{kpc} \lesssim 1$, the intensity for **TestC** is smaller than

in the optically thin case, where the intensity declines as $\propto D^{-2}$ due to geometrical dilution. This indicates that dense clumps absorb LW photons, and additional star formation may occur in the self-shielded regions for **TestC**. At $D \gtrsim 1$ kpc, the intensity roughly follows a profile $\propto D^{-2}$ for all the tests, but the intensity is the largest for **TestC**. LW radiation can quench star formation in low-mass MHs with intensities $J_{21} \gtrsim 0.1$ (O’Shea & Norman 2008). J_{21} exceeds this value in larger region of 3.84 kpc in **TestC**. Star formation may be delayed for \sim Myr in neighboring MHs due to strong LW emission from the star cluster.

At $D \sim 10$ kpc, the intensity rapidly declines for **TestA**, because the gas is optically thick in the LW band. For **TestB**, the gas remains optically thin, and the profile follows $\propto D^{-2}$. The local approximation with density gradient can safely estimate the column density in the D-front, but it fails to estimate the column density at larger distances $D \gtrsim 30$ kpc. Fortunately, at these distances, J_{21} is not so strong ($\sim 10^{-2}$), and thus star formation may not be significantly affected by this overestimate of J_{21} .

4.2.3 SN feedback

Massive Pop III stars will undergo SN explosions at the end of their lives and release the first metals into ISM and IGM. Chiaki et al. (2018) found that there are two modes of metal enrichment: internal enrichment (IE) and external enrichment (EE). The latter occurs if the emission rate of ionizing photons is sufficiently large before SN explosions occur. If an H II region expands beyond the virial radius of a host halo, SN shocks can propagate through the rarefied region without energy loss by radiative cooling. Therefore, EE occurs for a halo with masses below the critical value of Eq. (14).

For **TestA** and **B**, we can predict that, since the H II region will be bound in the MH, IE will occur. The ejected metal mass is $M_{\text{met}} \sim 1 M_{\odot}$ for a progenitor mass $M_{\text{PopIII}} \sim 10 M_{\odot}$ (Nomoto, Kobayashi, & Tominaga 2013). If the metals are uniformly mixed with the pristine gas with a mass $M_{\text{gas}} = 5 \times 10^4 M_{\odot}$ in the MH, the metallicity is estimated to be

$$Z_{\text{IE}} = \frac{M_{\text{met}}}{M_{\text{gas}}} = 10^{-3} Z_{\odot} \left(\frac{M_{\text{met}}}{1 M_{\odot}} \right) \left(\frac{M_{\text{gas}}}{5 \times 10^4 M_{\odot}} \right)^{-1} \quad (16)$$

as confirmed by earlier numerical studies (Ritter et al. 2012, 2015; Sluder et al. 2016; Chiaki & Wise 2019). For **TestC**, since the halo mass is below the critical mass, the cloud will be disrupted by multiple SN explosions. SN ejecta will reach neighboring halos. However, only a small fraction of ejecta can reach the center of the halos because of the pressure gradient force of gas clumps. Therefore, EE is expected to be less effective than IE. The resulting metallicity will be $Z_{\text{EE}} \lesssim 10^{-5} Z_{\odot}$ in the neighboring halos (Smith et al. 2015; Chen et al. 2017; Chiaki et al. 2018).

4.3 Caveats

4.3.1 HD photodissociation

In this work, we do not consider photodissociation of HD molecules, another important coolant in collapsing gas

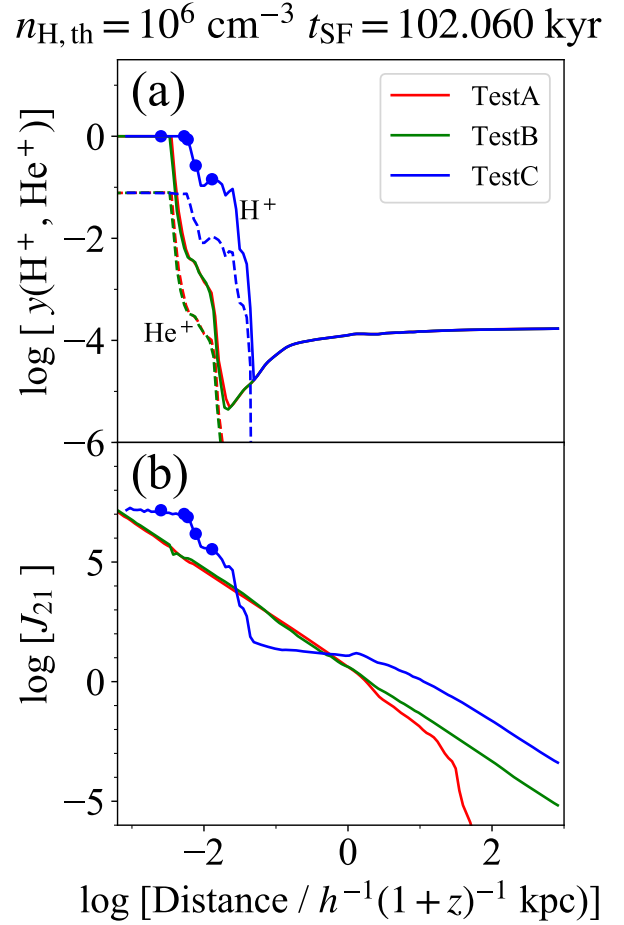


Figure 6. (a) Abundances of H^+ (solid curves) and He^+ (dashed curves) relative to hydrogen nuclei and (b) LW intensity J_{21} in units of $10^{-21} \text{ erg s}^{-1} \text{ cm}^{-2} \text{ Hz}^{-1} \text{ sr}^{-1}$ as a function of distance from the primary Pop III star at 100 kyr after the primary star formation. We take the average in each radial bin. The red, green and blue curves indicate the results for **TestA**, **TestB** and **TestC**, respectively. The blue circles denote the positions of the secondary stars for **TestC**.

clouds (Johnson & Bromm 2006; Hirano et al. 2014). HD molecules absorb photons in the LW band but in lines at different frequencies from H_2 . The gas is generally optically thin in the absorption lines, because the HD abundance is smaller than H_2 by five orders of magnitude (Omukai 2012). In our implementation, we assume that each photon package is monochromatic, and we use the shielding function (Eq. 8) averaged over all frequencies in the LW band (Wolcott-Green, Haiman, & Bryan 2011). HD molecules could receive only a fraction of photons that were not absorbed by H_2 . To overcome this problem, it is ideal to separate the photon package into three energy bins that interact with H_2 , HD and both. We will improve our model in forthcoming papers.

4.3.2 Stellar mass

We have fixed the primary star mass to $10.4 M_{\odot}$. The density and temperature structure of an H II region should change for different stellar masses (Kitayama et al. 2004; Whalen et al. 2008). For a more massive primary star, the density increases in a D-type front more rapidly because of the more intense ionizing photon emission. At the same time, the emission rate of LW photons is also larger, which may suppress the formation of the secondary stars. We will study star formation for a wider range of stellar masses in future work.

5 CONCLUSION

Massive stars emit tremendous amounts of ionizing photons, creating an H II region. At the limb of the H II region, a dense shell forms due to internal thermal pressure. This D-type front is a potential star-forming site (triggered star formation; Elmegreen & Lada 1977; Whitworth et al. 1994; Hosokawa & Inutsuka 2005, 2006). In this work, we find that star formation in the D-type front depends on the numerical scheme to solve LW radiation transport. The LW flux depends on the estimate of the H_2 column density N_{H_2} . We test three cases: the direct integration of H_2 density (TestA), local approximation based on the density gradient (TestB) and the Jeans length (TestC).

We compare the number of secondary stars forming in the D-type front. No secondary stars form in TestA and B while five stars form in TestC. In TestA, dissociating photons are only partially (~ 0.3) absorbed in a thin H_2 -ring, and the secondary star formation is suppressed. In Test B, the result is consistent with TestA, but we caution that the local approximation underestimates the column density. In TestC, the number of forming stars is overestimated because the Jeans length is generally larger than the thickness of the H_2 -ring.

It is numerically expensive to solve radiation transport of LW photons in numerical simulations because the gas is typically optically thin in the LW band, and photons can reach a large distance (~ 10 comoving kpc). In large-volume cosmological simulations with a side of \sim comoving Mpc, the local approximation is useful to reduce computational costs. We find that the computational time is reduced for the local approximation with the density gradient (TestB) by a factor of 2–3, compared to direct integration of N_{H_2} (TestA). Although the local approximation has limitations, the density gradient approach is a balanced strategy to reproduce the star formation history in the early stage of structure formation while keeping computational costs low.

ACKNOWLEDGMENTS

GC is supported by Research Fellowships of the Japan Society for the Promotion of Science (JSPS). JHW is supported by National Science Foundation grants OAC-1835213 and AST-2108020 and NASA grants NNX17AG23G, 80NSSC20K0520, and 80NSSC21K1053. The simulation was performed with NSF’s LRAC allocation AST-20007 on the Frontera resources in TACC. The figures in this paper are

constructed with the plotting library MATPLOTLIB (Hunter 2007).

DATA AVAILABILITY

The versions of ENZO, GRACKLE, and YT used in this work are available at <https://github.com/genchiaki/enzo-dev/tree/metal-dust>, <https://github.com/genchiaki/grackle/tree/metal-dust>, <https://github.com/genchiaki/yt/tree/metal-dust>, respectively. The script for YT used in this work is available at https://github.com/genchiaki/Analysis_CEMP. The simulation data will be shared on reasonable request to the authors.

REFERENCES

- Abel, T., Anninos, P., Zhang, Y., & Norman, M. L. 1997, *New Astron.*, 2, 181
- Abel, T., Bryan, G. L., & Norman, M. L. 2002, *Science*, 295, 93
- Behroozi P. S., Wechsler R. H., Wu H.-Y., 2013, *ApJ*, 762, 109. doi:10.1088/0004-637X/762/2/109
- Bromm, V., Coppi, P. S., & Larson, R. B. 1999, *ApJ*, 527, L5
- Brummel-Smith C., Bryan G., Butsky I., Corlies L., Emerick A., Forbes J., Fujimoto Y., et al., 2019, *JOSS*, 4, 1636. doi:10.21105/joss.01636
- Bryan G. L., Norman M. L., Stone J. M., Cen R., Ostriker J. P., 1995, *CoPhC*, 89, 149
- Bryan G. L., Norman M. L., 1997, arXiv, astro-ph/9710187
- Bryan, G. L., Norman, M. L., O’Shea, B. W., et al. 2014, *ApJS*, 211, 19
- Chen, K.-J., Whalen, D. J., Wollenberg, K. M. J., Glover, S. C. O., & Klessen, R. S. 2017, *ApJ*, 844, 111
- Chiaki, G., Yoshida, N., & Kitayama, T. 2013, *ApJ*, 762, 50
- Chiaki, G., Susa, H., & Hirano, S. 2018, *MNRAS*, 475, 4378
- Chiaki, G., & Wise, J. H. 2019, *MNRAS*, 482, 3933
- Draine, B. T., & Bertoldi, F. 1996, *ApJ*, 468, 269
- Efstathiou G., Davis M., White S. D. M., Frenk C. S., 1985, *ApJS*, 57, 241
- Elmegreen B. G., Lada C. J., 1977, *ApJ*, 214, 725. doi:10.1086/155302
- Federman S. R., Glassgold A. E., Kwan J., 1979, *ApJ*, 227, 466. doi:10.1086/156753
- Górski K. M., Hivon E., Banday A. J., Wandelt B. D., Hansen F. K., Reinecke M., Bartelmann M., 2005, *ApJ*, 622, 759. doi:10.1086/427976
- Greif, T. H., Bromm, V., Clark, P. C., et al. 2012, *MNRAS*, 424, 399
- Hartwig T., Glover S. C. O., Klessen R. S., Latif M. A., Volonteri M., 2015b, *MNRAS*, 452, 1233. doi:10.1093/mnras/stv1368
- Hahn, O., & Abel, T. 2011, *MNRAS*, 415, 2101
- Hirano, S., Hosokawa, T., Yoshida, N., et al. 2014, *ApJ*, 781, 60
- Hirano, S., Hosokawa, T., Yoshida, N., Omukai, K., & Yorke, H. W. 2015, *MNRAS*, 448, 568
- Hosokawa T., Inutsuka S.-. ichiro ., 2005, *ApJ*, 623, 917. doi:10.1086/428648
- Hosokawa T., Inutsuka S.-. ichiro ., 2006, *ApJ*, 646, 240. doi:10.1086/504789
- Hosokawa, T., Omukai, K., Yoshida, N., & Yorke, H. W. 2011, *Science*, 334, 1250
- Hunter J. D., 2007, *CSE*, 9, 90
- Jeon M., Besla G., Bromm V., 2021, *MNRAS*, 506, 1850. doi:10.1093/mnras/stab1771
- Johnson J. L., Bromm V., 2006, *MNRAS*, 366, 247. doi:10.1111/j.1365-2966.2005.09846.x

- Kitayama, T., Yoshida, N., Susa, H., & Umemura, M. 2004, *ApJ*, 613, 631
- Klein R. I., McKee C. F., Colella P., 1994, *ApJ*, 420, 213. doi:10.1086/173554
- Larson, R. B. 1969, *MNRAS*, 145, 271
- Magg M., Schauer A. T. P., Klessen R. S., Glover S. C. O., Tress R. G., Jaura O., 2022, *ApJ*, 929, 119. doi:10.3847/1538-4357/ac5aac
- Matsuda T., Satō H., Takeda H., 1969, *PThPh*, 42, 219. doi:10.1143/PTP.42.219
- Nakamura F., McKee C. F., Klein R. I., Fisher R. T., 2006, *ApJS*, 164, 477. doi:10.1086/501530
- Nomoto K., Kobayashi C., Tominaga N., 2013, *ARA&A*, 51, 457. doi:10.1146/annurev-astro-082812-140956
- Omukai, K. 2000, *ApJ*, 534, 809
- Omukai, K. 2001, *ApJ*, 546, 635
- Omukai K., 2012, *PASJ*, 64, 114. doi:10.1093/pasj/64.5.114
- O'Shea B. W., Norman M. L., 2008, *ApJ*, 673, 14. doi:10.1086/524006
- Peebles, P. J. E. 1980, Research supported by the National Science Foundation. Princeton, N.J., Princeton University Press, 1980. 435 p.,
- Planck Collaboration, Ade, P. A. R., Aghanim, N., et al. 2016, *A&A*, 594, A13
- Regan J. A., Wise J. H., O'Shea B. W., Norman M. L., 2020, *MNRAS*, 492, 3021. doi:10.1093/mnras/staa035
- Ricotti M., Gnedin N. Y., Shull J. M., 2001, *ApJ*, 560, 580. doi:10.1086/323051
- Ritter, J. S., Safraneck-Shrader, C., Gnat, O., Milosavljević, M., & Bromm, V. 2012, *ApJ*, 761, 56
- Ritter, J. S., Sluder, A., Safraneck-Shrader, C., Milosavljević, M., & Bromm, V. 2015, *MNRAS*, 451, 1190
- Safraneck-Shrader C., Krumholz M. R., Kim C.-G., Ostriker E. C., Klein R. I., Li S., McKee C. F., et al., 2017, *MNRAS*, 465, 885. doi:10.1093/mnras/stw2647
- Schauer A. T. P., Glover S. C. O., Klessen R. S., Clark P., 2021, *MNRAS*, 507, 1775. doi:10.1093/mnras/stab1953
- Schaerer, D. 2002, *A&A*, 382, 28
- Schneider, R., Ferrara, A., Salvaterra, R., Omukai, K., & Bromm, V. 2003, *Nature*, 422, 869
- Shull J. M., 1978, *ApJ*, 219, 877. doi:10.1086/155850
- Skinner D., Wise J. H., 2020, *MNRAS*.tmp, 126
- Sluder, A., Ritter, J. S., Safraneck-Shrader, C., Milosavljević, M., & Bromm, V. 2016, *MNRAS*, 456, 1410
- Smith, B. D., Wise, J. H., O'Shea, B. W., Norman, M. L., & Khochfar, S. 2015, *MNRAS*, 452, 2822
- Smith, B. D., Bryan, G. L., Glover, S. C. O., et al. 2017, *MNRAS*, 466, 2217
- Sobolev, V. V. 1960, Cambridge: Harvard University Press, 1960
- Stacy, A., Greif, T. H., & Bromm, V. 2012, *MNRAS*, 422, 290
- Sugimura K., Matsumoto T., Hosokawa T., Hirano S., Omukai K., 2020, *ApJL*, 892, L14. doi:10.3847/2041-8213/ab7d37
- Susa, H., Hasegawa, K., & Tominaga, N. 2014, *ApJ*, 792, 32
- Susa H., 2019, *ApJ*, 877, 99. doi:10.3847/1538-4357/ab1b6f
- Truelove, J. K., Klein, R. I., McKee, C. F., et al. 1997, *ApJ*, 489, L179
- Turk, M. J., Abel, T., & O'Shea, B. 2009, *Science*, 325, 601
- Turk M. J., Oishi J. S., Abel T., Bryan G. L., 2012, *ApJ*, 745, 154
- Turk M. J., Smith B. D., Oishi J. S., Skory S., Skillman S. W., Abel T., Norman M. L., 2011, *ApJS*, 192, 9
- Verner D. A., Ferland G. J., Korista K. T., Yakovlev D. G., 1996, *ApJ*, 465, 487
- Whalen, D., van Veelen, B., O'Shea, B. W., & Norman, M. L. 2008, *ApJ*, 682, 49
- Whitworth A. P., Bhattal A. S., Chapman S. J., Disney M. J., Turner J. A., 1994, *MNRAS*, 268, 291. doi:10.1093/mnras/268.1.291
- Wise, J. H., & Abel, T. 2011, *MNRAS*, 414, 3458
- Wise, J. H., Turk, M. J., Norman, M. L., & Abel, T. 2012, *ApJ*, 745, 50
- Wise J. H., Regan J. A., O'Shea B. W., Norman M. L., Downes T. P., Xu H., 2019, *Natur*, 566, 85. doi:10.1038/s41586-019-0873-4
- Wolcott-Green J., Haiman Z., Bryan G. L., 2011, *MNRAS*, 418, 838. doi:10.1111/j.1365-2966.2011.19538.x
- Wollenberg K. M. J., Glover S. C. O., Clark P. C., Klessen R. S., 2020, *MNRAS*, 494, 1871. doi:10.1093/mnras/staa289
- Woodward P., Colella P., 1984, *J. Comput. Phys.*, 54, 115
- Xu H., Wise J. H., Norman M. L., Ahn K., O'Shea B. W., 2016, *ApJ*, 833, 84. doi:10.3847/1538-4357/833/1/84
- Yoshida, N., Abel, T., Hernquist, L., & Sugiyama, N. 2003, *ApJ*, 592, 645
- Yoshida N., Oh S. P., Kitayama T., Hernquist L., 2007, *ApJ*, 663, 687. doi:10.1086/518227